Journal of Materials Chemistry A

PAPER

View Article Online
View Journal | View Issue

Cite this: J. Mater. Chem. A, 2017, 5, 12498

A hexanuclear cobalt metal–organic framework for efficient CO_2 reduction under visible light†

Jiao Zhao,‡ Qi Wang,‡ Chunyi Sun,* Tiantian Zheng, Likai Yan,* Mengting Li, Kuizhan Shao, Xinlong Wang* and Zhongmin Su

Increasing global challenges including climate warming and energy shortage have stimulated worldwide explorations for efficient materials for applications in the capture of CO_2 and its conversion to chemicals. In this study, a novel pillared-layer porous metal–organic framework (Co_6–MOF) with high nuclearity Co^{II} clusters has been synthesized. This material exhibited a CO_2 adsorption capacity of up to 55.24 cm^3 g^{-1} and 38.17 cm^3 g^{-1} at 273 K and 298 K, respectively. In a heterogeneous photocatalytic system of CO_2 reduction, this material, co-operated with a ruthenium-based photosensitizer, can efficiently realize CO_2 to CO conversion. Under visible-light irradiation for 3 hours, 39.36 μmol CO and 28.13 μmol H_2 were obtained. This result is higher than those of most of the reported MOF materials under similar conditions and to the best of our knowledge, this is the first example of a high nuclear MOF used in CO_2 reduction. The rooted reasons behind the high reactivity were studied through theoretical calculation studies. The results showed that electrons on reduced $[Ru(bpy)_3]Cl_2 \cdot 6H_2O$ (bpy = 4,4′-bipyridine) could transfer to the Co_6–MOF and the adsorbed CO_2 molecule on the charged Co_6–MOF could be activated more facilely. This work not only clarifies the reasons for high efficiency of the CO_2 photoreduction system but also points out to us the direction for designing more effective MOF materials as photocatalysts for artificial CO_2 photoreduction.

Received 24th March 2017
Accepted 13th May 2017

DOI: 10.1039/c7ta02611k

rsc.li/materials-a

Introduction

In recent years, climate warming has become a global environmental problem which primarily results from excessive emissions of CO_2 from fossil fuel combustion.[1–3] To solve this issue, tremendous efforts have been devoted to reducing CO_2 concentration in air. CO_2 capture and sequestration (CCS) technologies using porous materials as sorbent materials are an accepted and working approach.[4–6] One kind of the outstanding porous material in this field is metal–organic frameworks (MOFs) which are constructed from organic ligands and metal ions or metal clusters. Benefiting from large surface areas and tailorable structures, these hybrid porous materials show intriguing applications in various fields including chemical separation,[7] catalysis,[8] drug delivery,[9] optical sensing detection,[10] and gas storage,[11,12] particularly in CO_2 capture.[1] The CO_2 adsorption of MOF materials is related to their pore size and shape, surface characteristics and porous functionalities. One promising strategy for increasing CO_2 adsorption is to introduce N-rich aromatic ligands.[13]

Beyond the CCS route, the catalytic transformation of the captured CO_2 into value-added chemicals could be a more suitable alternative and sustainable method as CO_2 represents an abundant and inexpensive carbon source.[11–13] Owing to the chemical inertness of the CO_2 molecule, reducing it into chemical feedstocks needs high energy and appropriate catalysts.[14–17] Utilizing clean and renewable solar energy as the power source to accomplish this conversion could be the most economical and environmentally friendly choice.[18] Therefore, the exploration of high-performance photocatalytic systems for CO_2 reduction has been the fundamental goal of experts. In photocatalytic systems, there are three essential steps to achieve the transition from solar energy to chemical energy,[19–22] including light harvesting, generation of electron–hole pairs, and transferring redox equivalents to reactive centers for redox reactions. Noble metal complexes, such as Ru and Re complexes, are widely utilized as light harvesters in various photocatalytic systems, including water splitting[23–25] and CO_2 reduction.[26–29] Transition metals with multiple redox states and organic ligands are essential to form electron-transport chains together with light harvesters accelerating CO_2 reduction. For instance, cobalt complexes and oxides have been reported to

Institute of Functional Material Chemistry, National & Local United Engineering Laboratory for Power Batteries, Key Laboratory of Polyoxometalate Science of Ministry of Education, Northeast Normal University, Changchun, 130024 Jilin, People's Republic of China. E-mail: suncy009@nenu.edu.cn; wangxl824@nenu.edu.cn; Fax: +86-431-85684009; Tel: +86-431-85099108

† Electronic supplementary information (ESI) available: Schemes, figures and CIF files giving selected bonds and angles, PXRD, TGA. CCDC 1533801. For ESI and crystallographic data in CIF or other electronic formats see DOI: 10.1039/c7ta02611k

‡ These authors contributed equally to this work.

serve as co-catalysts enhancing CO_2 photoconversion through boosting charge separation and surface reaction.[30,31] In addition to the three aspects above, for the gaseous reactions, adsorption and activation of CO_2 molecules are especially crucial in practical applications since effective charge transfer between catalytic centers and CO_2 molecules lies in their intimate and stable binding.[31] Therefore, in the process of CO_2 reduction, it is important to combine the adsorption and activation of CO_2 with transition-metal catalysis. Transition-metal MOFs with excellent capability for CO_2 adsorption might be materials with incomparable advantage in CO_2 reduction. Employing a classical cobalt-containing MOF material, Co-ZIF-9 (ZIF = zeolitic imidazolate framework), as a co-catalyst[27] and $[Ru(bpy)_3]Cl_2 \cdot 6H_2O$ as a photosensitizer, Wang *et al.* reported an efficient CO_2 reduction system under visible light. In spite of this, the design and synthesis of a kind of MOF material with excellent capability for CO_2 adsorption meanwhile maintaining the highly matched energy band with a photosensitizer is a significant challenge.[32–35] What's more, the mechanism in such CO_2 reduction systems needs to be revealed.

Herein, we report the synthesis of a hexanuclear cobalt-cluster MOF $[Co_3(OH)_3(NTB)(4,4'\text{-bpy})_{1.5}]$ DEF (Co_6–MOF, NTB = 4,4′,4″-nitrilotribenzoic acid ligands, 4,4′-bpy = 4,4′-bipyridine, and DEF = *N*,*N*-diethylformamide), in which the 2D layer is constituted by $Co_6(\mu_3\text{-}OH)_6$ clusters and NTB and the pillar is the 4,4′-bpy ligand. This novel porous material acting as a heterogeneous co-catalyst exhibits efficient CO_2 photochemical reduction by cooperating with a ruthenium-based photosensitizer. Under visible-light irradiation for 3 hours, 39.36 μmol CO and 28.13 μmol H_2 were obtained. Based on the theoretical calculation, the reaction mechanism was studied which indicated that the excited electrons can be efficiently transferred from the lowest unoccupied molecular orbital (LUMO) of the ruthenium-based photosensitizer to the LUMO of the hexanuclear cobalt-cluster MOF. And after accepting electrons, the activation of the CO_2 molecule is facilitated by the charged Co_6–MOF.

Experimental section

Materials

$Co(CH_3CHO)_2 \cdot 6H_2O$, NTB and 4,4′-bpy for the synthesis were purchased from Alfa, and they were used as received. The purity of all reagents was of analytical grade.

Instrumentation

The C, H and N elemental analyses were performed on a Perkin-Elmer 2400 CHN elemental analyzer. The FT-IR spectra were examined in the range of 4000–400 cm^{-1} on a Mattson Alpha-Centauri spectrometer using KBr pellets. The UV-Vis absorption spectra were acquired on a Shimadzu UV-2550 spectrophotometer in the wavelength range of 200–800 nm. Powder X-ray diffraction (PXRD) patterns were collected with an X-ray diffractometer of Rigaku, Rint 2000. Thermogravimetric analyses (TGA) were carried out on a Perkin-Elmer TG-7 analyzer heated from room temperature to 1000 °C under a nitrogen gas atmosphere at a heating rate of 5 °C min^{-1}.

Synthesis of $[Co_3(NTB)\ (4,4'\text{-bpy})_{1.5}(OH)_3] \cdot$ DEF (Co_6–MOF)

A solid mixture of NTB (30.0 mg, 0.080 mmol), 4,4′-bpy (15.6 mg, 0.100 mmol), and $Co(CH_3CHO)_2 \cdot 6H_2O$ (37.4 mg, 0.150 mmol) was suspended in DEF (diethylformamide, 6 mL) in a 25 mL Teflon-lined stainless steel container. The mixture was heated at 120 °C for 2 days resulting in red crystals, which were washed and isolated using DMF. Subsequently, they were dried in air at room temperature. The yield of the Co_6–MOF violet crystals was 78% based on NTB. Elemental analyses: anal. calcd (%) for $C_{41}H_{38}N_5O_{10}Co_3$, calculated (%): C 52.52; H 4.09; N 7.47. Found (%): C 52.55; H 4.11; N 7.43. Selected IR (KBr pellet, cm^{-1}): 532.29(w), 582.05(w), 633.28(w), 667.37(w), 709.96(w), 784.19(m), 816.01(w), 1008.66(w), 1096.91(w), 1174.40(w), 1220.58(w), 1275.12(m), 1313.54(s), 1398.86(s), 1505.31(m), 1541.36(s), 1595.64(s), 1664.80(s), 2927.58(w), 3394.84(w), 3742.00(w), 3858.87(w).

X-ray crystallography study

Single-crystal X-ray diffraction data for the Co_6–MOF were recorded by using a Bruker Apex CCD diffractometer with graphite-monochromated Mo Kα radiation (λ = 0.71069 Å) at 293 K. Absorption corrections were applied using a multi-scan technique. All the structures were solved by the direct method of SHELXS-2014 and refined by full-matrix least-squares techniques using the SHELXL-2014 program within WinGX. Non-hydrogen atoms were refined with anisotropic temperature parameters. CCDC 1533801 for the Co_6–MOF contains the supplementary crystallographic data for the work.†

Gas sorption experiments

The N_2 and CO_2 sorption measurements were performed on automatic volumetric adsorption equipment (Belsorp mini II). The solvent-removal assay has been employed before the gas adsorption measurements. The fresh as-synthesized samples were immersed in CH_2Cl_2 for 48 h, and then transferred to CH_3OH for 48 h to remove the DEF. Subsequently, the samples were gathered by decanting CH_2Cl_2 similarly to remove CH_3OH. When the CH_2Cl_2 was removed by decanting, these samples were activated by heating under a dynamic vacuum at 100 °C for 24 h to form the activated samples. Before the gas adsorption test, the samples needed to be dried again by using the 'outgas' function of the surface area analyzer for 12 h at 150 °C. After activation, the samples were tested for N_2 and CO_2 sorption measurements.

Photocatalytic test

Photocatalytic reactions were carried out in a quartz tube with a cap at 1 atm CO_2 partial pressure. The reaction system contained $[Ru(bpy)_3]Cl_2 \cdot 6H_2O$ (0.01 mmol), Co_6–MOF (0.005 mmol), acetonitrile (4 mL), H_2O (1 mL), and triethanolamine (TEOA 1 mL). After the solution was purified by CO_2 for 10 min, it was beamed by a 150 W xenon lamp at $420 \leq \lambda \leq 780$ nm in

a carousel irradiation apparatus. The reaction temperature was maintained at 35 °C by using a water bath. The result of PXRD shows that at the end of the reaction, the crystal retains the original structure (Fig. S11†). After the catalytic reaction completed, the gases (CO and H_2) were tested and analyzed using a GC instrument. To detect the formation of carbon monoxide from the reaction mixture, 500 μL from the middle of the test tube was taken out with a syringe and injected into a GC with a FID detector, using argon as the carrier gas and reference gas. The volume of the carbon monoxide produced was calculated by comparing the integrated area of the signals of carbon monoxide with a calibration curve. The injector and detector temperatures were set to 60 °C. The retention time of hydrogen was 1.9 min. To detect the formation of hydrogen from the reaction mixture, 1000 μL of the headspace of the test tube was taken out with a syringe and injected into a GC with a TCD detector, using a 5 Å molecular sieve column and argon as the carrier gas and reference gas. The volume of the hydrogen produced was calculated by comparing the integrated area of the signals of hydrogen with a calibration curve. The injector and detector temperatures were set to 60 °C. The retention time of hydrogen was 0.7 min. All the photocatalytic reactions were repeated five times to confirm the reliability of the data.

Results and discussion

Crystal structures

The Co_6–MOF was prepared through admixing 4,4′-bpy, NTB ligands and $Co(CH_3CHO)_2 \cdot 6H_2O$ in DEF heated at 120 °C for 2 days. The reaction produced violet crystals with a polyhedral morphology. The structures of the Co_6–MOF were confirmed by single X-ray crystallography. Single-crystal X-ray diffraction analysis reveals that the Co_6–MOF crystallized in the hexagonal $P6_3/mcm$ space group (Table S2†). In the asymmetric unit, there are a half Co ion, one-sixth NTB ligands and one-fourth 4,4′-bpy ligands. The solvent DEF molecules in the channels are not crystallographically well defined. Six Co cations and six μ_3-OH groups construct $Co_6(\mu_3\text{-OH})_6$ clusters serving as secondary building units (SBUs) in the structure. Each Co ion in the $Co_6(\mu_3\text{-OH})_6$ clusters adopts six coordination connecting with one nitrogen atom of the 4,4′-bpy ligand and five oxygen atoms provided by two carboxylates of different NTB ligands and three μ_3-OH groups (Fig. 1(a)). Besides, each 4,4′-bpy ligand binds to two Co atoms in two $Co_6(\mu_3\text{-OH})_6$ SBUs through N atoms in the 4,4′-position (Fig. S1†). Each NTB ligand act as a 3-connecting node linked with three $Co_6(\mu_3\text{-OH})_6$ SBUs forming two-dimensional layers (Fig. S2†). The adjacent $Co_6(\mu_3\text{-OH})_6$–NTB layers are further pillared by the bpy triangular prism (Fig. 1(a)), constituting an overall 3D columnar supporting structure (Fig. S5†). It is worth noting that such a triangular prism pillared-layer structure enhanced the stability of the architecture. The pillared layer structure contains three different types of channel continuity along a, b and c axes (Fig. 1(b), (c) and S3†) with the dimensions of 11.31 × 12.56 Å ($a \times c$ or $b \times c$) (Fig. S4(a)†) and 8.89 × 8.89 Å ($a \times b$) (Fig. S4(b)†). Topological analysis shows that the $Co_6(\mu_3\text{-OH})_6$ SBUs can be regarded as 8-connected nodes, and the NTB ligand was defined as a 3-connected node, so the architecture of the Co_6–MOF can be reduced to a 3,8-connected tfz-d (α-UO_3) type topology with the point symbol of $(4^3)_2(4^6.6^{18}.8^4)$ (Fig. 1(d)). Many MOFs with the tfz-d type topology have been reported.[36–38] In this type of topology, 3-connected and 8-connected nodes exist simultaneously, and they will form a double connected 3D structure. PLATON calculation shows that the effective pore volume of the Co_6–MOF is about 63.9% (4682.8 $Å^3$) per unit cell (7324.9 $Å^3$), which is occupied by DEF molecules.

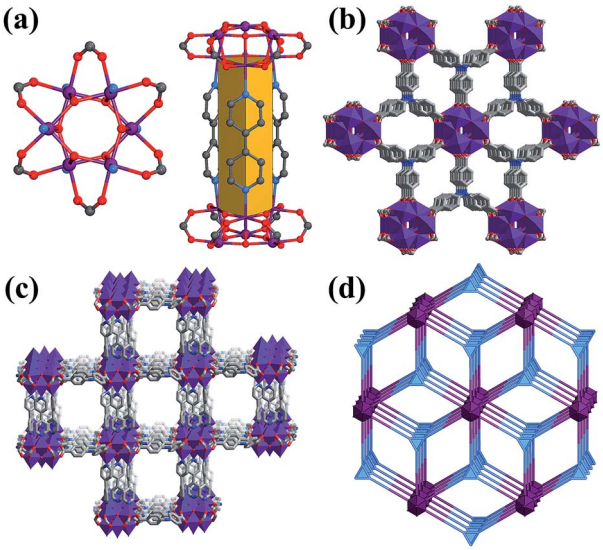

Fig. 1 (a) The coordination environment of $Co_6(\mu_3\text{-OH})_6$ SBUs. (b) and (c) Ball-and-stick model of the carbon nanotube channel along the [$a \times b$] and [$a \times c$ or $b \times c$] directions. (d) Topological nets of the Co_6–MOF. All hydrogen atoms and solvent molecules have been omitted for clarity. Color coding: Co: violet; C: gray; O: red; N: sky blue.

Chemical and thermal stability

The purity of the synthesized Co_6–MOF was verified by high similarities between simulated and experimental powder X-ray diffraction (PXRD) patterns. In order to determine the possibility of the practical application of the Co_6–MOF, we investigated its stability toward moisture. The PXRD patterns still exhibit high similarities compared with simulated PXRD patterns after soaking in water for 24 h. In addition, the acid resistance and alkali resistance of the Co_6–MOF were also investigated. Surprisingly, after placing it in a hydrochloric acid solution (pH = 2) and sodium hydroxide solution (pH = 12) for 24 h, it exhibits excellent acid and alkali resistance revealed by the similar shape and intensity of the PXRD (Fig. S6†). Such high acid resistance and alkali resistance are quite rare in reported MOFs.[39] The thermal stability of the Co_6–MOF is revealed through the TG curve. As shown in Fig. S7,† an evident weight loss of 11.2% was observed in the step from 270 to 285 °C, which may be ascribed to the release of solvent molecules. After 285 °C, the framework of the Co_6–MOF starts to decompose.

Gas adsorption properties

To study the porosity and CO_2 adsorption capability of the Co_6–MOF, we performed the N_2 and CO_2 adsorption experiments

(Fig. 2). The samples were adequately activated by the method represented in the Experimental section. The PXRD of the activated sample showed similar peaks to the as-synthesized sample, indicating the maintenance of the framework.

N_2 adsorption of the activated Co_6–MOF was carried out at 77 K. The adsorption isotherm of N_2 unfolds a characteristic type I behavior with good reversibility for microporous solids. The Brunauer–Emmett–Teller (BET) and Langmuir surface areas are 1957.5 $m^2\ g^{-1}$ and 2257.1 $m^2\ g^{-1}$, respectively, calculated using the N_2 adsorption isotherms, and the total pore volume of the Co_6–MOF is 0.87 $cm^3\ g^{-1}$. The N_2 adsorption amount of the Co_6–MOF at 1 bar is approximately 568.1 $cm^3\ g^{-1}$, which is equivalent to 42.1 N_2 per unit cell, lower than the theoretical pore volume calculated using PLATON based on the single crystal X-ray diffraction data. In order to prove that the Co_6–MOF structure remains intact in water, we performed N_2 sorption of the Co_6–MOF which was soaked in water for 24 h. The corresponding adsorption isotherm of this sample is presented in Fig. S9† and the result shows that its BET surface area is similar to that of the activated sample indicating that the structure of the Co_6–MOF is maintained well after being soaked in water.

The CO_2 sorption behaviors of the Co_6–MOF were measured at 273 K and 298 K, respectively, and the sorption isotherms are shown in Fig. 2(b). At 1 atm and 273 K, the Co_6–MOF has CO_2 uptakes at a saturation of 55.24 $cm^3\ g^{-1}$, based on the total weight. And at 298 K, the CO_2 uptakes decreased slightly, up to 38.17 $cm^3\ g^{-1}$ (Fig. 2(b)). This capacity is comparable to classical MOFs Uio-66 and NH_2-Uio-66 which were employed as catalysts for CO_2 reduction.[40]

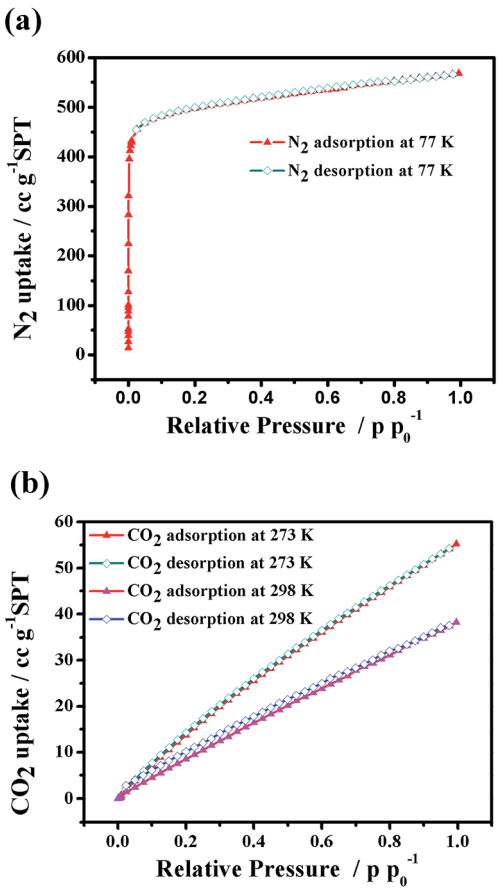

Fig. 2 (a) N_2 sorption isotherms of the Co_6–MOF; (b) CO_2 sorption isotherms of the Co_6–MOF.

Photochemical CO_2 reduction properties

The photocatalytic CO_2 reduction system consists of Co_6–MOF, $[Ru(bpy)_3]Cl_2\cdot 6H_2O$, and TEOA (triethanolamine). The solvents of the photocatalytic system filled with atmospheric CO_2 are MeCN and H_2O. After irradiation with visible light ($\lambda \geq 420$ nm) for 30 min, the reduction system generated CO (3.73 μmol) and H_2 (2.81 μmol) gases. In this reduction process, CO_2 was split into CO at a reaction rate of 0.13 μmol min^{-1}, along with the evolution of H_2 at a rate of 0.10 μmol min^{-1} (Fig. 3). Trace CH_3OH was detected in the solution. With increasing reaction time, the evolution amount of CO and H_2 enhances consistently (Fig. 3). After 3 hours' irradiation, the total amount of CO and H_2 reaches 39.35 and 28.13 μmol (entry 1, Table 1). This activity is much higher than those of many classical MOF materials for converting CO_2 to CO listed in Table S1.†[20,27] The photochemical quantum yield of CO (Φ_{CO}) of the Co_6–MOF under irradiation of 420 nm light was calculated as 0.758% (the detailed calculation is given in the ESI†).

In order to determine the importance of the components in the photocatalytic CO_2 reduction system, we provided a series of reference experiments and the results are summed up in Table 1. As we have seen, in total darkness, CO or H_2 was undetectable in the photocatalytic system (entry 2, Table 1). When the system was short of $[Ru(bpy)_3]Cl_2\cdot 6H_2O$, no gases were detected in the reaction system (entry 3, Table 1). Replacing $[Ru(bpy)_3]Cl_2\cdot 6H_2O$ with tris(2-phenylpyridinato)iridium(III), CO gas wasn't detected in the reaction while only a trace amount of H_2 was produced (entry 13, Table 1). These results mentioned above indicate the necessity of the energy band matching of the photosensitizer and MOFs in the photocatalytic CO_2 reduction reaction. This was further ascertained by the fact that no CO or

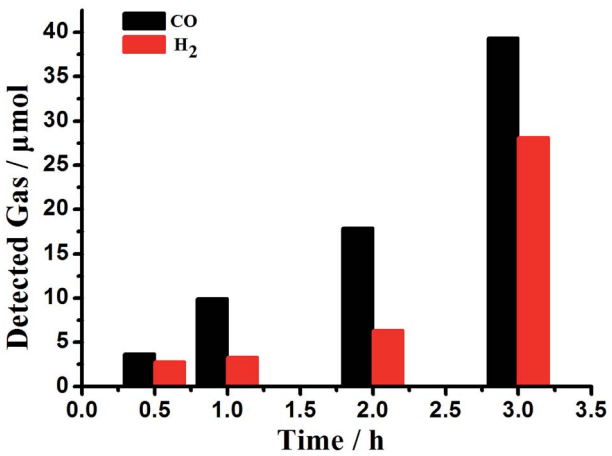

Fig. 3 The effect of the reaction time on the evolution of CO and H_2 from the CO_2 photoreduction system.

Table 1 The research of reaction conditions[a]

Entry	CO [μmol]	H_2 [μmol]	TON[b]
1	39.36	28.13	13.50
2[c]	n.d.[d]	n.d.	n.d.
3[e]	n.d.	n.d.	—
4[f]	10.46	6.39	3.37
5[g]	27.64	13.97	8.29
6[h]	13.6	5.61	3.84
7[i]	n.d.	2.37	0.47
8[j]	n.d.	n.d.	—
9[k]	29.23	9.98	7.84
10[l]	n.d.	n.d.	—
11[m]	15.11	63.96	15.81
12[n]	11.74	20.53	6.45
13[o]	n.d.	0.61	0.12
14[p]	16.56	2.80	3.87

[a] Reaction conditions: $[Ru(bpy)_3]Cl_2 \cdot 6H_2O$ (0.01 mmol), Co_6–MOF (0.005 mmol, activated), acetonitrile (MeCN, 4 mL), H_2O (1 mL), TEOA (1 mL), CO_2 (1 atm), $\lambda \geq 420$ nm, 35 °C, 3 h. [b] Turnover number (mol amount of CO and H_2)/(mol amount of Co_6–MOF). [c] In the dark. [d] Not detectable. [e] Without $[Ru(bpy)_3]Cl_2 \cdot 6H_2O$. [f] Without the Co_6–MOF. [g] The Co_6–MOF was destroyed by calcination at 900 °C in N_2 gas. [h] Using 4,4′-bpy, NTB, and $Co(CH_3CHO)_2 \cdot 6H_2O$ to replace the Co_6–MOF. [i] Using N_2 to replace CO_2. [j] Without TEOA. [k] Using TEA instead of TEOA. [l] Without MeCN. [m] Without H_2O. [n] Using DMF (*N*,*N*-dimethylformamide) to replace MeCN. [o] Using tris(2-phenylpyridinato)iridium(III) instead of $[Ru(bpy)_3]Cl_2 \cdot 6H_2O$. [p] Using Co_3O_4-Uio-66 to replace the Co_6–MOF.

H_2 was detected when the photosensitizer didn't exist or when the band mismatch of the photosensitizer and MOFs occurred.

In the experimental study, we also explored the influence of the amount of Co_6–MOF on the photocatalytic properties in the system (Fig. 4). In this figure, we can see that the yield of CO and H_2 changed obviously when the added amount of Co_6–MOF changed a little. The optimum amount of Co_6–MOF is 3 mg with maximum values of both CO and H_2. Overall, these results have proved the major role of the Co_6–MOF by fastening CO_2 acting as a CO_2 redox promoter and an absorber in the photocatalytic reduction system.

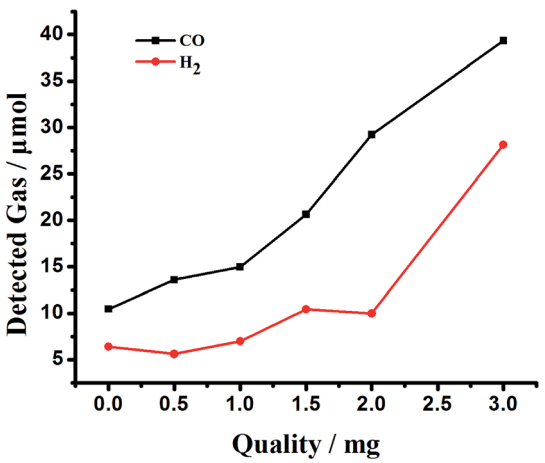

Fig. 4 The effect of the amount of Co_6–MOF on the evolution of CO and H_2 from the CO_2 photoreduction system.

In the absence of the Co_6–MOF, the turnover number decreases to 3.37, which is significantly lower than that of the catalytic system containing $[Ru(bpy)_3]Cl_2 \cdot 6H_2O$ and Co_6–MOF (entry 4, Table 1). To further confirm the role of the formation of MOFs as a co-catalyst in the photocatalytic reaction system, we destroyed the Co_6–MOF by calcination at 900 °C in N_2 gas, and then the residues were applied in the reaction system instead of the Co_6–MOF (entry 5, Table 1). The results showed that CO and H_2 production decreased dramatically. This indicates the necessity of the complete framework structure of the Co_6–MOF in the CO_2 splitting, possibly by the promotion of substrate concentration and carrier transfer. To further confirm the role of the formation of MOFs as a co-catalyst in the photocatalytic reaction system, we measured the photocatalytic efficiency of physical mixtures including Co^{2+} and the ligand in a homogeneous system. We use 4,4′-bpy, NTB, and $Co(CH_3CHO)_2 \cdot 6H_2O$ to replace the Co_6–MOF, and the result reflected that their physical mixture also plays a catalytic role in the photocatalytic reaction system, but with a lower TON than those with the Co_6–MOF (entry 6, Table 1). These results noted above confirmed that as a heterogeneous co-catalyst, the Co_6–MOF effectively promotes the efficiency of the photochemical reaction.

In the experiment of photocatalytic reaction, the participation of CO_2 was investigated by replacing CO_2 with N_2 (entry 7, Table 1). Once CO_2 was replaced by N_2, the evolution of CO was not observed, and only 2.37 μmol H_2 was detected under the same reaction conditions. It is noticeable that when there was no CO_2 in the system, light-induced electrons could just promote H_2 generation.

In the course of the experiment, we found that the reaction medium has a great influence on the catalytic effect of the Co_6–MOF on the CO_2 photocatalytic reduction reaction. No reaction occurred when only H_2O was used as the reaction medium which might be due to the weak chemical affinity towards CO_2 molecules (entry 10, Table 1). Meanwhile, MeCN and DMF were favorable reaction media for the CO_2 reduction (entry 11 and entry 12, Table 1). They possessed nitrogen or oxygen atoms that can interact with and solubilize CO_2 *via* Lewis acid–base interactions.[41,42] In addition, we replaced the Co_6–MOF with Co_3O_4-Uio-66 and the turnover number (3.87) decreased, becoming significantly lower than that of the original catalytic system (entry 14, Table 1 and Fig. S13†).

In order to unambiguously determine the source of the C atom of CO, we conducted an isotopic tracing experiment by replacing CO_2 by $^{13}CO_2$ under the same photocatalytic reaction conditions, and we used gas chromatography mass spectrometry to analyse the evolution of CO. After irradiation with visible light for 30 min, the peak at 1.99 min and m/z 29 was assigned to ^{13}CO (Fig. S12†) and no sign at m/z 28 was detected. It turns out to be the case that the Co_6–MOF can indeed stimulate the deoxygenative reduction of CO_2 to CO.

The results above clearly demonstrate the effective role of the Co_6–MOF in the photocatalytic system. The next important target is to understand the root reason in such a system. Inspired by Tang's work,[43] the highest occupied molecular orbital (HOMO) and the lowest unoccupied molecular orbital (LUMO) energy levels of the $[Ru(bpy)_3]Cl_2$ photosensitizer and

Co_6–MOF are studied first. According to ref. 43 the HOMO and LUMO of $[Ru(bpy)_3]Cl_2$ are −5.68 and −3.19 eV, respectively. Theoretical calculation is introduced to reveal the HOMO and LUMO of the Co_6–MOF. The calculation result shows the HOMO and LUMO of the Co_6–MOF to be −6.22 and −4.56 eV (Fig. S14†). Since the LUMO of the Co_6–MOF is lower than that of $[Ru(bpy)_3]Cl_2$, the electrons in the LUMO of $[Ru(bpy)_3]Cl_2$ can be transferred to the LUMO of the Co_6–MOF (Fig. 5).

As described above, the Co_6–MOF has the capability of CO_2 adsorption, and the adsorption energy was investigated as well. As the density functional theory (DFT) calculation shows, the adsorption energy of the Co_6–MOF in CO_2 adsorption is 0.275 eV since the activation of the CO_2 molecule is usually triggered by two-electron charges.[44] From first-principles simulations, we calculated the adsorption energy changes after the Co_6–MOF accepted one or two electrons. The result shows that when receiving one electron, the energy increases from 0.275 to 0.361 eV. When obtaining two electrons, the energy further enhances to 0.907 eV. What's more, we simulated the potential energy surfaces with the variation of the O–C bond of CO_2 adsorbed on the Co_6–MOF. From the simulation results, we can see that one-electron charge can hardly change the activation energy barrier (E_B) of CO_2 while two-electron charge can effectively reduce the E_B from 5.66 to 4.98 eV (Fig. 5(c) and S15†). Therefore, upon receiving electrons from the $[Ru(bpy)_3]Cl_2$ photosensitizer, the Co_6–MOF can turn into an active photocatalyst material for the CO_2 activation further facilitating CO_2 reduction.

On the basis of the above results, a possible rooted reason for CO_2 reduction in the Co_6–MOF participated system was proposed. Under irradiation, the photosensitizer $[Ru(bpy)_3]Cl_2$ is excited to the excited state. This excited state was then quenched reductively by the sacrificial electron donor, TEOA[40] (Fig. 5(a)), and formed a reduced photosensitizer. Then the electrons in the reduced photosensitizer transferred to the Co_6–MOF. The adsorbed CO_2 molecule on the Co_6–MOF was activated after the Co_6–MOF obtained the electrons. In the end, CO_2 is reduced to CO and released from the Co_6–MOF.

Conclusions

In conclusion, based on highly symmetrical $Co_6(\mu_3\text{-}OH)_6$ cluster SBUs and organic ligands of NTB and 4,4′-bpy, a pillared-layer hexanuclear cobalt MOF, Co_6–MOF, was obtained possessing a nanoporous structure. With this merit, the Co_6–MOF displays a satisfactory amount of CO_2 uptake, up to 55.24 $cm^3\ g^{-1}$. Under

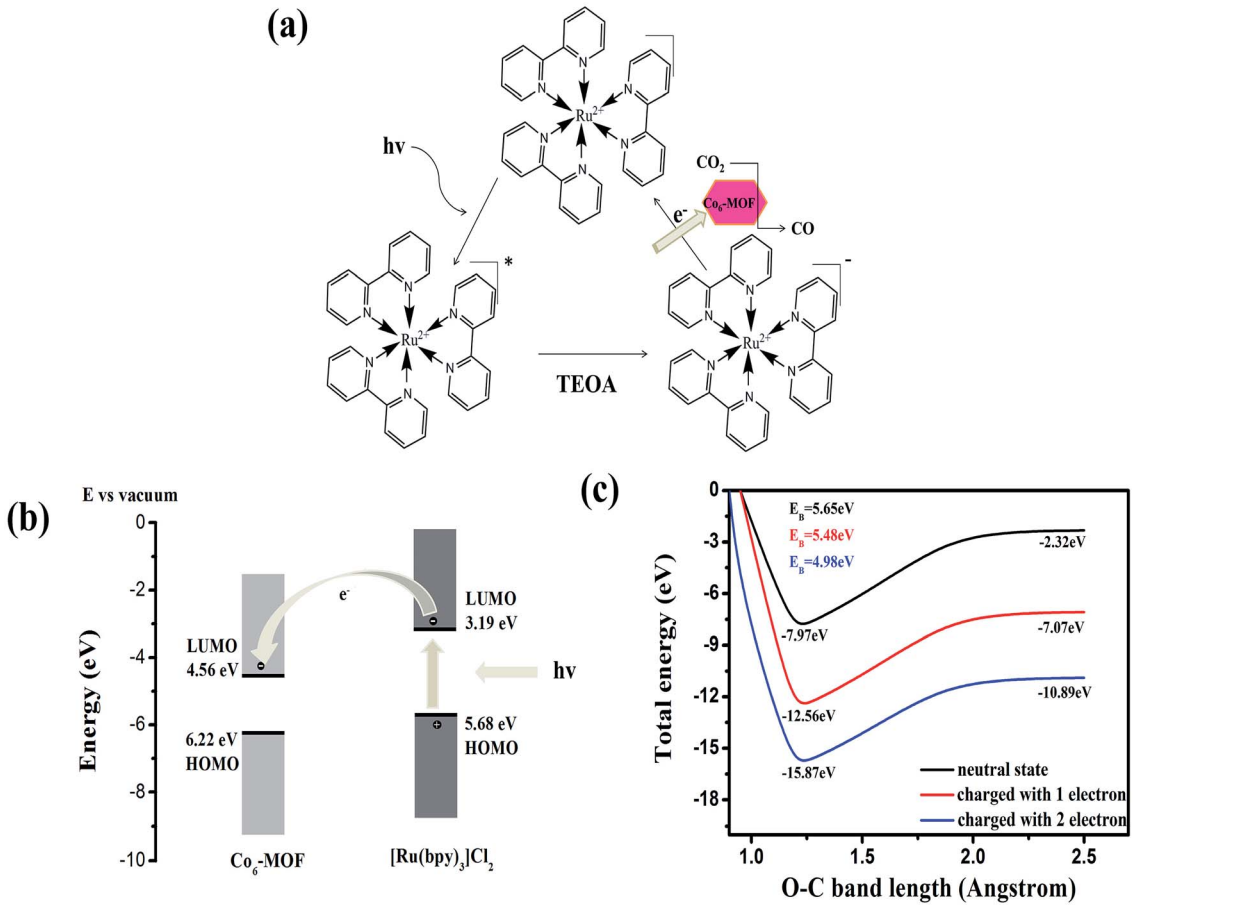

Fig. 5 (a) Proposed mechanism of the photosensitized catalytic reduction of CO_2 to CO. (b) Schematic energy-level diagram showing electron transfer from $[Ru(bpy)_3]Cl_2$ to the Co_6–MOF. (c) Potential energy surfaces along the O–C bond length for the activation of the CO_2 molecule adsorbed on the Co_6–MOF in the neutral state or the states charged with one or two electrons, from which the E_B of CO_2 were deducted.

irradiation with visible light, the Co_6–MOF can be used as a stable co-catalyst coupled to an appropriate photosensitizer ($[Ru(bpy)_3]Cl_2 \cdot 6H_2O$) realizing the photocatalytic reduction of CO_2 to CO. Around 39.36 μmol CO and 28.13 μmol H_2 were produced after 3 hours of irradiation. This result is higher than those of most of the reported classic MOF materials under similar conditions. To the best of our knowledge, this is the first example of the use of a high nuclear MOF in CO_2 reduction. A possible mechanism was proposed through theoretical calculation studies. The results showed that electrons on reduced $[Ru(bpy)_3]Cl_2 \cdot 6H_2O$ could transfer to the Co_6–MOF and the adsorbed CO_2 molecule on the charged Co_6–MOF could be activated more facilely. The rooted reasons behind the high reactivity were revealed through theoretical calculation studies which showed that electrons on reduced $[Ru(bpy)_3]Cl_2 \cdot 6H_2O$ could transfer to the Co_6–MOF and the adsorbed CO_2 molecule on the charged Co_6–MOF could be activated more facilely. This work not only clarifies the reasons for the high efficiency of the CO_2 photoreduction system but also points out to us the direction for designing more effective MOF materials as photocatalysts for artificial photochemical CO_2 reduction.

Acknowledgements

This work was financially supported by the NSFC of China (No. 21601032, 21671034, and 21471027), National Key Basic Research Program of China (No. 2013CB834802), Fundamental Research Funds for the Central Universities (2412016KJ021), Changbai Mountain Scholars of Jilin Province, and Foundation of Jilin Educational Committee (No. 2016498).

Notes and references

1 C. C. Wang, Y. Q. Zhang, J. Li and P. Wang, *J. Mol. Struct.*, 2015, **1083**, 127–135.
2 J. Albo, P. Luis and A. Irabien, *Ind. Eng. Chem. Res.*, 2010, **49**, 11045–11051.
3 T. Ohno, N. Murakami, T. Koyanagi and Y. Yang, *J. CO_2 Util.*, 2014, **6**, 17–25.
4 J. R. Li, J. Yu, W. Lu, L. B. Sun, J. Sculley, P. B. Balbuena and H. C. Zhou, *Nat. Commun.*, 2013, **4**, 1538–1545.
5 S. Sato, T. Morikawa, T. Kajino and O. Ishitani, *Angew. Chem., Int. Ed.*, 2013, **52**, 988–992.
6 W. Wang, S. Wang, X. Ma and J. Gong, *Chem. Soc. Rev.*, 2011, **40**, 3703–3727.
7 J. R. Li, R. J. Kuppler and H. C. Zhou, *Chem. Soc. Rev.*, 2009, **38**, 1477–1504.
8 J. Y. Lee, O. K. Farha, J. Roberts, K. A. Scheidt, S. T. Nguyen and J. T. Hupp, *Chem. Soc. Rev.*, 2009, **38**, 1450–1459.
9 C. Y. Sun, C. Qin, C. G. Wang, Z. M. Su, S. Wang, X. L. Wang, G. S. Yang, K. Z. Shao, Y. Q. Lan and E. B. Wang, *Adv. Mater.*, 2011, **23**, 5629–5632.
10 C. Y. Sun, W. P. To, X. L. Wang, K. T. Chan, Z. M. Su and C. M. Che, *Chem. Sci.*, 2015, **6**, 7105–7111.
11 K. Sumida, D. L. Rogow, J. A. Mason, T. M. McDonald, E. D. Bloch, Z. R. Herm, T. H. Bae and J. R. Long, *Chem. Rev.*, 2012, **112**, 724–781.
12 M. Alvaro, E. Carbonell, B. Ferrer, F. X. Llabrés i Xamena and H. Garcia, *Chem.–Eur. J.*, 2007, **13**, 5106–5122.
13 J. S. Qin, D. Y. Du, W. L. Li, J. P. Zhang, S. L. Li, Z. M. Su, X. L. Wang, Q. Xu, K. Z. Shao and Y. Q. Lan, *Chem. Sci.*, 2012, **3**, 2114–2118.
14 H. Takeda, K. Koike, H. Inoue and O. Ishitani, *J. Am. Chem. Soc.*, 2008, **130**, 2023–2031.
15 J. Grodkowski, T. Dhanasekaran, P. Neta, P. Hambright, B. S. Brunschwig, K. Shinozaki and E. Fujita, *J. Phys. Chem. A*, 2000, **104**, 11332–11339.
16 Y. H. Fu, D. R. Sun, Y. J. Chen, R. K. Huang, Z. X. Ding, X. Z. Fu and Z. H. Li, *Angew. Chem.*, 2012, **124**, 3420–3423.
17 P. L. Feng, J. J. Perry IV, S. Nikodemski, B. W. Jacobs, S. T. Meek and M. D. Allendorf, *J. Am. Chem. Soc.*, 2010, **132**, 15487–15489.
18 K. Garg, Y. Matsubara, M. Z. Ertem, A. Lewandowska-Andralojc, S. Sato, D. J. Szalda, J. T. Muckerman and E. Fujita, *Angew. Chem., Int. Ed.*, 2015, **54**, 14128–14132.
19 D. R. Sun, Y. H. Fu, W. J. Liu, L. Ye, D. K. Wang, L. Yang, X. Z. Fu and Z. H. Li, *Chem.–Eur. J.*, 2013, **19**, 14279–14285.
20 R. Li, J. H. Hu, M. S. Deng, H. L. Wang, X. J. Wang, Y. L. Hu, H. L. Jiang, J. Jiang, Q. Zhang, Y. Xie and Y. J. Xiong, *Adv. Mater.*, 2014, **26**, 4783–4788.
21 H. W. Huang, J. J. Lin, G. B. Zhu, Y. X. Weng, X. X. Wang, X. Z. Fu and J. L. Long, *Angew. Chem., Int. Ed.*, 2016, **55**, 1.
22 S. N. Habisreutinger, L. Schmidt-Mende and J. K. Stolarczyk, *Angew. Chem.*, 2013, **125**, 7516–7557.
23 Y. Baia, L. Q. Yea, L. Wang, X. Shia, P. Q. Wang, W. Baia and P. K. Wong, *Appl. Catal., B*, 2016, **194**, 98–104.
24 S. B. Wang, J. L. Lin and X. C. Wang, *Phys. Chem. Chem. Phys.*, 2014, **16**, 14656–14660.
25 L. N. Li, S. Q. Zhang, L. J. Xu, J. Y. Wang, L. X. Shi, Z. N. Chen, M. C. Hong and J. H. Luo, *Chem. Sci.*, 2014, **5**, 3808–3813.
26 G. Sahara and O. Ishitani, *Inorg. Chem.*, 2015, **54**, 5096–5104.
27 S. B. Wang, W. S. Yao, J. L. Lin, Z. X. Ding and X. C. Wang, *Angew. Chem., Int. Ed.*, 2014, **53**, 1034–1308.
28 S. Sato, T. Arai and T. Morikawa, *Inorg. Chem.*, 2015, **54**, 5105–5113.
29 J. R. Li, J. Sculley and H. C. Zhou, *Chem. Rev.*, 2012, **112**, 869–932.
30 J. Lin, Z. Pan and X. Wang, *ACS Sustainable Chem. Eng.*, 2014, **2**, 353–358.
31 S. B. Wang, J. L. Lin and X. C. Wang, *Phys. Chem. Chem. Phys.*, 2014, **16**, 14656–14660.
32 A. Dhakshinamoorthy, A. M. Asiri and H. García, *Angew. Chem., Int. Ed.*, 2016, **55**, 5414–5445.
33 H. Q. Xu, J. H. Hu, D. K. Wang, Z. H. Li, Q. Zhang, Y. Luo, S. H. Yu and H. L. Jiang, *J. Am. Chem. Soc.*, 2015, **137**, 13440–13443.
34 H. Zhang, J. Wei, J. Dong, G. Liu, L. Shi, P. An, G. Zhao, J. Kong, X. Wang, X. Meng, J. Zhang and J. Ye, *Angew. Chem., Int. Ed.*, 2016, **55**, 14310–14314.
35 Y. Su, Z. Zhang, H. Liu and Y. Wang, *Appl. Catal., B*, 2017, **200**, 448–457.
36 M. O'Keeffe, M. A. Peskov, S. J. Ramsden and O. M. Yaghi, *Acc. Chem. Res.*, 2008, **41**, 1782–1789.

37 S. J. Garibay, J. R. Stork, Z. Q. Wang, S. M. Cohen and S. G. Telfer, *Chem. Commun.*, 2007, **46**, 4881–4883.
38 F. Luo, Y. X. Che and J. M. Zheng, *Cryst. Growth Des.*, 2008, **8**, 2006–2010.
39 X. L. Hu, C. Y. Sun, C. Qin, X. L. Wang, H. N. Wang, E. L. Zhou, W. E. Li and Z. M. Su, *Chem. Commun.*, 2013, **49**, 3564–3566.
40 D. R. Sun, Y. H. Fu, W. J. Liu, L. Ye, D. K. Wang, L. Yang, X. Z. Fu and Z. H. Li, *Chem.–Eur. J.*, 2013, **19**, 14279–14285.
41 L. Pan, D. H. Olson, L. R. Ciemnolonski, R. Heddy and J. Li, *Angew. Chem.*, 2006, **118**, 632–635.
42 Y. Matsubara, E. Fujita, M. D. Doherty, J. T. Muckerman and C. Creutz, *J. Am. Chem. Soc.*, 2012, **134**, 15743–15757.
43 C. Gao, Q. Q. Meng, K. Zhao, H. J. Yin, D. W. Wang, J. Guo, S. L. Zhao, L. Chang, M. He, Q. X. Li, H. J. Zhao, X. J. Huang, Y. Gao and Z. Y. Tang, *Adv. Mater.*, 2016, **28**, 6485–6490.
44 T. Inoue, A. Fujishima, S. Konishi and K. Haonda, *Nature*, 1979, **227**, 637.